CHEMISTRY
A EUROPEAN JOURNAL

DOI: 10.1002/chem.200902144

Adsorption of CO_2, CH_4, and N_2 on Zeolitic Imidazolate Frameworks: Experiments and Simulations

Javier Pérez-Pellitero,[a] Hedi Amrouche,[a, b] Flor R. Siperstein,[b] Gerhard Pirngruber,[c] Carlos Nieto-Draghi,*[a] Gérald Chaplais,[d] Angélique Simon-Masseron,[d] Delphine Bazer-Bachi,[c] David Peralta,[c, d] and Nicolas Bats[c]

Abstract: Experimental measurements and molecular simulations were conducted for two zeolitic imidazolate frameworks, ZIF-8 and ZIF-76. The transferability of the force field was tested by comparing molecular simulation results of gas adsorption with experimental data available in the literature for other ZIF materials (ZIF-69). Owing to the good agreement observed between simulation and experimental data, the simulation results can be used to identify preferential adsorption sites, which are located close to the organic linkers. Topological mapping of the potential-energy surfaces makes it possible to relate the preferential adsorption sites, Henry constant, and isosteric heats of adsorption at zero coverage to the nature of the host–guest interactions and the chemical nature of the organic linker. The role played by the topology of the solid and the organic linkers, instead of the metal sites, upon gas adsorption on zeolite-like metal–organic frameworks is discussed.

Keywords: adsorption · host–guest systems · metal–organic frameworks · topochemistry · zeolite analogues

Introduction

The recent appearance of metal–organic frameworks (MOFs) has generated a vast volume of studies and attracted the attention of an important part of the scientific community. The possibility of tailoring these materials in terms of pore size[1] or group functionalities makes them extremely attractive for a wide variety of applications such as CO_2 storage, alkylation catalysis, or alkylbenzene separation. The so-called zeolitic imidazolate frameworks (ZIFs)[2–5] are a particularly interesting class of MOFs. ZIFs are constructed from tetrahedral units formed by one bivalent metal M^{2+} cation (usually Zn^{2+}) and four imidazolate anions (Im^-). Because of the strong bonding between the imidazolate linker and the metal center, many ZIFs have high thermal (>673 K) and moisture stability compared with many other MOF structures.[6] The $\{M^{2+}(Im^-)_2\}$ units are analogous to the $\{SiO_2\}$ tetrahedra in zeolites and the M-Im-M bond angle is similar to the Si-O-Si bond angle. It is, therefore, possible to form zeolite-like networks from these building units. ZIF analogues have been found for gmelinite (GME), sodalite (SOD), Linde Type A (LTA), and rho (RHO) zeolite topologies, among others.

The M–Im–M units in ZIFs are longer than the Si–O–Si (or Si–O–Al) units in a zeolite. Therefore, the cavities of ZIF materials are generally much larger than those of the corresponding zeolites. Consequently the pore volume is also much larger (provided that the cavities of the ZIF are accessible). The combination of a large pore volume with a pore size in the subnanometer range translates into a potentially high adsorption capacity, which has been experimen-

[a] Dr. J. Pérez-Pellitero, H. Amrouche, Dr. C. Nieto-Draghi
Department of Thermodynamic and Molecular Simulation
IFP 1 et 4, Avenue de Bois-Préau
2852 Rueil-Malmaison Cedex (France)
Fax: (+33) 1-47527058
E-mail: carlos.nieto@ifp.fr

[b] H. Amrouche, Dr. F. R. Siperstein
School of Chemical Engineering and Analytical Science
The University of Manchester, PO Box 88, Sackville Street
Manchester M60 1QD (UK)

[c] Dr. G. Pirngruber, Dr. D. Bazer-Bachi, D. Peralta, Dr. N. Bats
Department of Catalysis and Separation
IFP BP3, 69360 Solaize Cedex (France)

[d] Dr. G. Chaplais, Dr. A. Simon-Masseron, D. Peralta
Equipe Matériaux à Porosité Contrôlée (MPC)
Institut de Science des Matériaux de Mulhouse (IS2M)
LRC CNRS 7228, Université de Haute Alsace (UHA)
ENSCMu, 3 rue Alfred Werner
68093 Mulhouse Cedex (France)

Supporting information for this article is available on the WWW under http://dx.doi.org/10.1002/chem.200902144.

tally confirmed.[2,7–10] Moreover, it is possible to tune the affinity of ZIFs for adsorbate molecules by modifying the imidazolate linkers by introducing different substituents or functional groups. The applicability of this concept was recently demonstrated by Banerjee et al.[11] They prepared a series of ZIFs with the same GME topology but with chemically different imidazolate linkers and different pore sizes. Thus, they were able to tune the adsorption capacity of CO_2 as well as the CO_2/CH_4 and CO_2/N_2 selectivity from respectably high values down to values close to those for an activated carbon material. The adsorption capacity and selectivity are related to both the affinity of the imidazolate linker for CO_2 and the pore size of the ZIF (which, in turn, is determined by the steric demands of the linker).

If the topology is not fixed (as in the study of Banerjee et al.), it will be an additional variable that has an impact on the adsorption capacity and selectivity of ZIFs. In practice it is not easy to dissociate the effects of topology, pore size, and chemical nature of the linker because the first two factors indirectly depend on the last: the molecular structure of the linker directs the synthesis towards a certain pore size and topology. Here molecular simulation can help to analyze how the complex interplay of linker, pore size, and topology affects the adsorption behavior of ZIFs. Molecular simulation separates and quantifies the contributions of the three parameters cited above; thereby it provides a possible explanation and may lead to predictions of the adsorption behavior of ZIFs.

Numerous force-field-based Monte Carlo (MC) simulation studies of adsorption have already been carried out for MOF materials. Without an exhaustive search of all the simulation studies of adsorption in MOFs, most of the work published deals with the IRMOFs (isoreticular MOFs),[12–17] MILs (materials of the Institut Lavoisier),[18–20] and [Cu_3-(BTC)$_2$] (BTC = benzene-1,3,5-tricarboxylate).[21,22] With few exceptions,[20,23] no dedicated force-field development took place in these studies, but standard material force fields (Dreiding,[24] universal force field (UFF),[25] or consistent valence force field (CVFF))[26] were used. The standard force fields seem to reproduce the physical properties of MOF materials fairly well. Dedicated force fields in MOF materials for the analysis of structural properties have been developed.[27,28] Since grand canonical MC simulations were not carried out in these last studies, it is not yet possible to analyze their suitability to describe gas adsorption isotherms.

As mentioned above, the added value of molecular simulation is that it allows us to analyze the factors that determine the shape of the adsorption isotherms. It was used to identify the preferred adsorption sites, to establish correlations between adsorption capacities and pore size and pore volume of different MOF structures, and to evaluate the contribution of electrostatic and van der Waals (vdW) forces to the overall adsorption potential.[12–14,17,29] ZIF materials have received significantly less attention than other MOF structures with carboxylate linkers. Liu et al. studied the adsorption of CO_2 on ZIF-68 and ZIF-69 by using MC simulations to determine equilibrium properties and molecular dynamics to calculate self-diffusivities.[30] ZIF-68 and ZIF-69 have the same topology (GME), but are constructed by using different linkers.

In this work we studied the adsorption of three different gases (CO_2, CH_4, and N_2) on three ZIF structures with different topologies and compositions: ZIF-8 (SOD topology), ZIF-76 (LTA topology), and ZIF-69 (GME topology). The influence of the pore structure and the way the chemical nature of the linker affected the adsorption were analyzed. The structural properties of the ZIF materials are summarized in Table 1. Their structures and the organic linkers used in their synthesis are shown in Figure 1. In ZIF-8, sodalite cages (free diameter = 1.16 nm) are connected by six-membered rings, that is, windows with six Zn atoms. The imidazolate linkers point towards the center of the six-membered ring, which connects two sodalite cages. The free diameter of the opening of the six-membered ring is, therefore, only 0.34 nm. This is smaller than the kinetic diameter of CH_4, but because the opening is not spherical and because there is probably some flexibility in the structure, the window is just large enough to allow CO_2, N_2, and CH_4 to diffuse into the pores of ZIF-8. Framework ZIF-8 has a smaller experimental porosity and a higher experimental surface area and pore volume per gram of crystal than the other two ZIFs.

Table 1. Topology and textural properties of the ZIFs analyzed in this work.

ZIF	Linker	Topology	d_p [nm][a]	d_w [nm][b]	S_a [$m^2 g^{-1}$][c] exptl/calcd	ϕ[d] exptl/calcd	V_p[e] [$cm^3 g^{-1}$] exptl/calcd
ZIF-8	mIm	SOD[f]	1.16	0.34	1445/1413	0.35/0.48	0.59/0.52
ZIF-69	nIm/cbIm	GME[g]	0.78	0.44	950/1029	NA/0.56[h]	0.34/0.48
ZIF-76	Im/cbIm	LTA[i]	1.22	0.54	1340/1620	0.47/0.66	0.57/0.80

[a] Pore diameter. [b] Accessible diameter of window. [c] Surface area. [d] Porosity. [e] Pore volume. [f] Sodalite cages directly connected by six-membered-ring windows. [g] Twelve-membered-ring channel cages delimited by eight- and six-membered rings. [h] NA: experimental data not available. [i] Sodalite cages connected by double four-membered rings.

Framework ZIF-69 has the most complex pore structure (GME topology). It has two one-dimensional pores, one built from 12-membered rings and the other from six-membered rings. β-Chlorobenzoimidazole organic linkers point to the center of the 12-membered rings, reducing the free diameter of this ring from 1.5 nm to 0.78 nm. The six-membered rings consist of nIm linkers, with the nitro groups pointing away from the center of the ring. The free diameter of the six-membered ring is, therefore, comparable to that of ZIF-8.[1] In theory, the two channel systems could be connected through eight-membered rings, but the openings are obstructed by the nitro groups. Note also that the six-membered ring is connected by three double four-membered rings that are not permeable to molecules, but which create

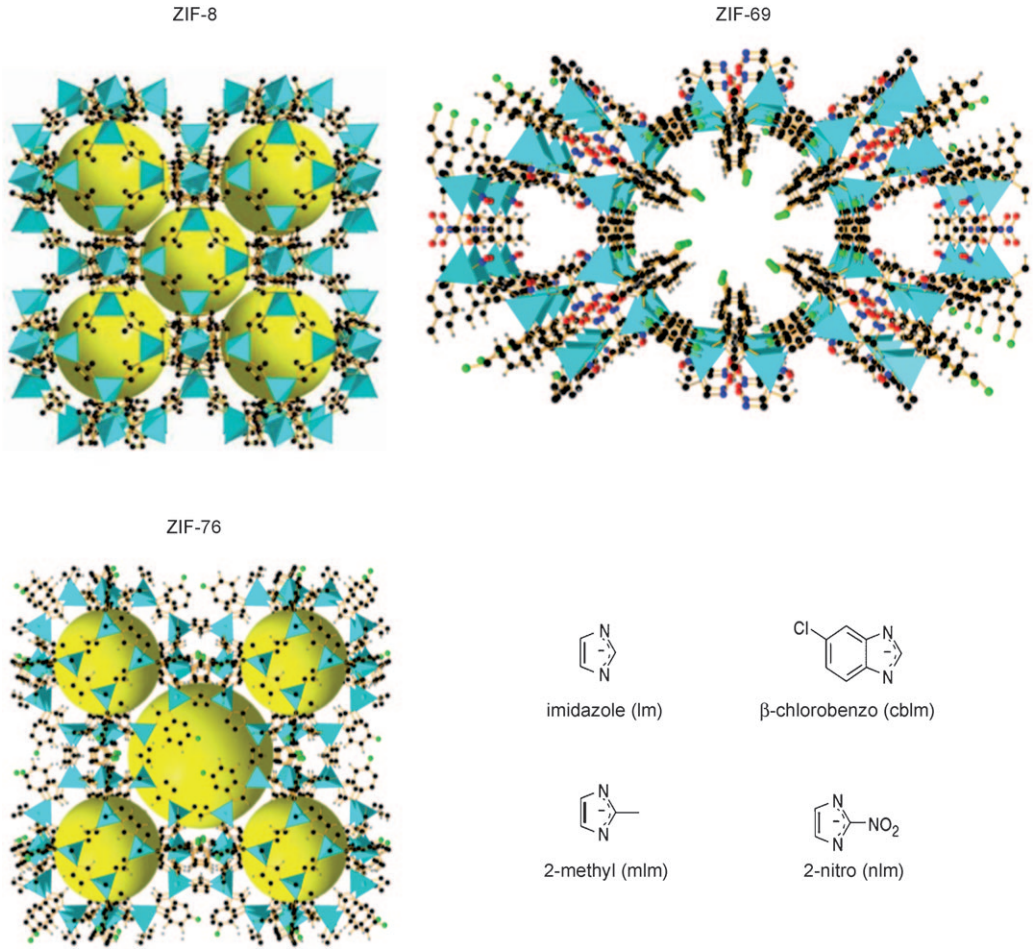

Figure 1. Crystal structures and imidazole (Im) organic linkers of the ZIFs.

three side-pockets in each segment of the six-membered-ring channel. Framework ZIF-69 has the smallest experimental surface area and porous volume of the three materials analyzed in this work.

In the LTA topology (i.e., ZIF-76), large cages are connected by eight-membered rings. Each large cage is surrounded by eight smaller sodalite cages at the corners of a cube. The sodalite cages are interconnected by double four-membered rings. Molecules can enter the sodalite cage from the large cage through a six-membered ring opening. In ZIF-76, some of the cbIM linkers point towards the center of the eight-membered ring connecting two large cages. The six-membered-ring window is occupied by Im and cbIm linkers. Because the position of the chlorine atoms is disordered, it is difficult to estimate the diameter of the opening of the eight-membered-ring window. In any case, the opening is large enough for CO_2, CH_4, and N_2 molecules to diffuse in (which is not the case in zeolite A). The experimental surface area and porous volume in this solid are slightly lower than in ZIF-8.

Two of the solids (ZIF-8 and ZIF-76) were synthesized and were experimentally studied in this work. Published adsorption data were used for ZIF-69 and compared with the MC simulations. First, several force fields were validated by comparing experimental and simulation data for ZIF-8. As previously noticed by Fairen-Jimenez et al.,[31] the standard force fields previously cited considerably overestimate the available experimental isotherms. We, therefore, adjusted the standard UFF parameters by scaling their intermolecular parameters (see computational methods in the Experimental Section for details). The transferability of the readjusted force field was successfully tested by comparing the simulation results with experimental adsorption isotherms of N_2, CO, CH_4, and CO_2 on ZIF-76 and ZIF-69 (additional comparisons are provided in the Supporting Information for H_2 adsorption on ZIF-8 and ZIF-11).

In a second step we analyzed the preferential adsorption sites by means of potential-energy surfaces computed from vdW and electrostatic interactions. The role played by the electrostatic interactions and the metal atoms in the ZIF structures was also analyzed. Finally, the thermodynamic behavior of N_2, CH_4, and CO_2 adsorbed on ZIF-8, ZIF-69, and ZIF-76 was compared through Henry constants and the isosteric heats of adsorption.

Results and Discussion

Force-field optimization: Experimentally measured adsorption isotherms of methane on ZIF-8 at 303 K and those obtained from simulations are compared in Figure 2. Adsorption isotherms measured in this work were in agreement with the data reported by Zhou et al.[7] Figure 2 also contains the adsorption isotherms calculated by using two force fields available in the literature and the force field developed in this work.

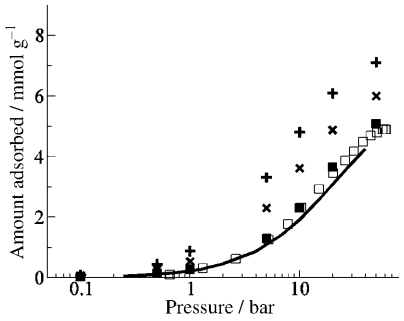

Figure 2. Comparison of the experimental methane isotherm at 303 K with the isotherms obtained with different intermolecular potential force fields on ZIF-8 (□ = experimental data from Ref. [7] at 300 K, —— = experiments during this work, ■ = simulations during this work, + = simulations by using UFF and × = Dreiding force fields).

The agreement between the two sets of experiments and our simulation results with the new force field is valid for the whole range of pressures for the adsorption of CH_4. We have obtained a scaling factor of $\xi \approx 0.51$, which reflects an important reduction of the vdW cohesive energy of CH_4 with respect to the original UFF. This is in agreement with the previous simulation results reported in Ref. [31] for ZIF-8. We then used this factor to adjust the dispersion repulsion parameters for the additional atoms needed to describe host–guest interactions of different gases adsorbed on different ZIFs materials as described in [Eq. (1)].

$$\sigma_{UFF}^{New} = 0.95\sigma_{UFF}$$
$$\varepsilon_{UFF}^{New} = 0.69\varepsilon_{UFF} \quad (1)$$

The general validity of these adjusted force-field parameters of the host material was tested by comparing the simulation results with the new experimental adsorption isotherms of N_2 and CO_2 in Figure 3. The agreement observed between both sets of results is remarkably good over the whole range of pressures. No additional adjustments were made to the force-field parameters, either for N_2 and CO_2 data shown in Figure 3 or for the rest of the systems studied in this work. The final set of force-field parameters is listed in the Supporting Information.

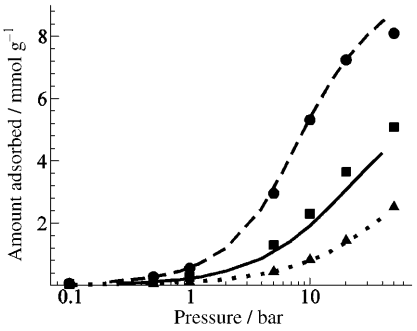

Figure 3. Comparison of experimental N_2 and CO_2 isotherms in ZIF-8 at 303 K with the simulation results obtained with the optimized force field. The experiments are denoted by lines (•••• = N_2, —— = CH_4, and – – – = CO_2) and the simulations by symbols (▲ = N_2, ■ = CH_4, and ● = CO_2).

Force-field transferability: Because we intend to deduce the general trends in gas-adsorption behavior on zeolite-like metal organic frameworks, the transferability of our force field has been tested by comparing the simulation results obtained by using the optimized force field with the experimental measurements for N_2, CH_4, and CO_2 adsorption on ZIF-76 at 303 K in Figure 4.

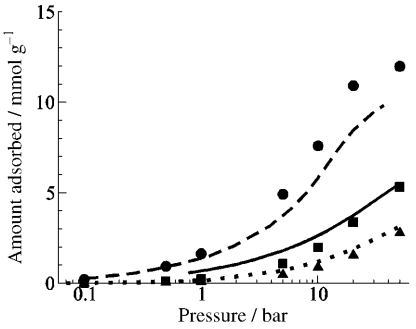

Figure 4. Comparison of experimental N_2, CH_4, and CO_2 isotherms on ZIF-76 at 303 K with the simulations obtained with the optimized force fields. The experiments are denoted by lines (•••• = N_2, —— = CH_4, and – – – = CO_2) and the simulations by symbols (▲ = N_2, ■ = CH_4, and ● = CO_2).

In general, as in the case of ZIF-8, we observe a fairly good agreement between the experimental adsorption isotherms and the simulation results. Although CO_2 is overestimated at high pressure and CH_4 is underestimated at low pressure, we consider the agreement satisfactory, given that no further parameter adjustment was made. Nevertheless, N_2 adsorption is reproduced well by our simulations. Finally, we have tested our force field by comparing the simulation results with other adsorption data available in the literature and have obtained good agreement with the experimental adsorption data for CO_2, CO, and CH_4 isotherms of ZIF-69[1,11] at 273 K (Figure 5). Additional comparisons of H_2 adsorption on ZIF-8 and ZIF-11[8] at 77 K are provided in the Supporting Information.

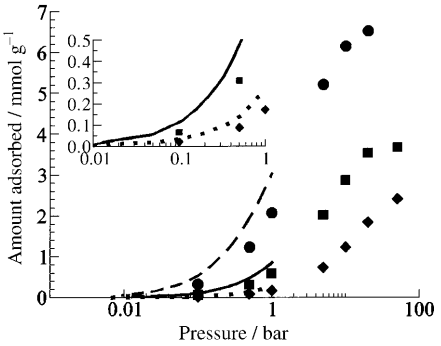

Figure 5. Comparison of molecular simulation results with the experimental data on CO_2 and CO gas adsorption on ZIF-69 at 273 K (Ref. [12]). The experiments are denoted by lines (•••••= CO, ——= CH_4, and – – –= CO_2) and the simulations by symbols (◆= CO, ■= CH_4, and ●= CO_2). Inset: The low-pressure range for CH_4 and CO up to 1 bar.

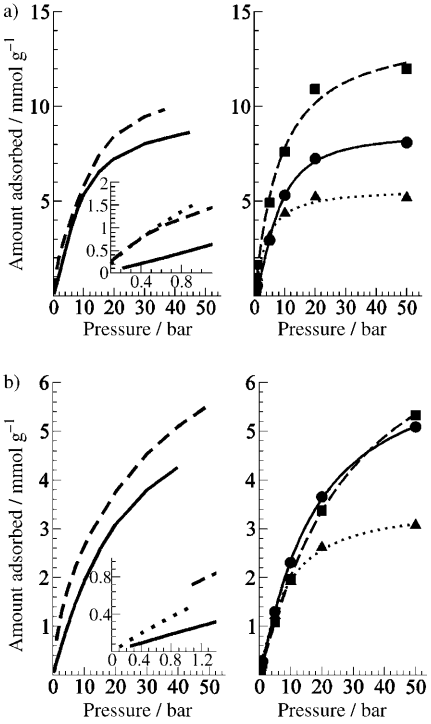

Figure 6. Comparison of experimental (left) and simulation (right) adsorption isotherms at 303 K for a) CO_2 and b) CH_4 for ZIF-8 (——, ●), ZIF-69 (•••••, ▲), and ZIF-76 (– – –, ■). For the simulation data, the lines connecting the symbols are Freundlich–Langmuir fittings. Experimental data for ZIF-69 up to 1 bar is taken from Ref. [11] at 298 K. Inset: The low pressure range for CO_2 (a) and CH_4 (b) up to 1 bar.

It is interesting that the standard force fields (UFF and Dreiding) showed an overestimation of the host–guest interactions with a deviation of more than 66% at 1 bar for CO_2 and CH_4 isotherms on ZIF-69 (see the Supporting Information for details). This disagreement is similar to that previously observed for gas adsorption on ZIF-8 by using these force fields. A recent study successfully reproduces the experimental CO_2 isotherm on ZIF-69 and ZIF-68 with MC simulation by using the original UFF.[30] The discrepancy between our results and those for CO_2 reported in these works may come from the different techniques employed to obtain the electrostatic charge distribution for the ZIF framework. In general, we have higher charges on Zn metal (1.1 e) and NO_2 groups (O: −0.48 e, N: 0.57 e) and lower charges on H atoms (0.14 e) than the values reported in Ref. [30].

The comparison between our simulation results and the experimental data for different gases (N_2, CH_4, CO, CO_2) adsorbed on different solids (ZIF-8, ZIF-69, ZIF-76) confirms the quality of the proposed force field for adsorption predictions.

Analysis of the adsorption behavior: Figure 6 compares the experimental and simulated adsorption isotherms of CO_2 and CH_4 of the three ZIFs at 303 K. The simulations predict that the quantities of CO_2 adsorbed at high pressure increase in the order ZIF-69 < ZIF-8 < ZIF-76, which corresponds to the order of the pore volumes of the samples. The trend found in the simulations was experimentally confirmed for ZIF-76, which adsorbed more CO_2 than ZIF-8 throughout the pressure range. The difference between ZIF-76 and ZIF-8 is smaller than in the simulations. This difference could be attributed to the fact that the actual measured pore volume of ZIF-76 was smaller than the theoretical value. In the low-pressure region, ZIF-76 and ZIF-69 adsorb similar quantities in both simulation and experiments (see Figure 6, insets), and the isotherm of ZIF-8 is significantly lower.

The order of the simulated isotherms of CH_4 at low pressure is ZIF-69 > ZIF-8 > ZIF-76. At very high pressure, the order changes and follows the pore volumes of the samples, as in the case of CO_2. The order of the experimental isotherms is different. In contrast to the simulations, ZIF-76 adsorbs more CH_4 than ZIF-8. We tentatively attribute this to the scaling factor of the dispersive energy, $\xi = 0.51$, which led to an underestimation of the vdW interactions with the cbIm ring of ZIF-76. This hypothesis is supported by the observation that our simulations slightly underestimate the adsorption capacities of ZIF-69, which also contains the cbIm linker (see Figure 5). In spite of having identified this problem, we preferred to maintain our philosophy of using a unique correction factor of the cohesive energy for all linkers, instead of optimizing it for each material. This practice will preserve the transferability of the force field to testing gas adsorption on ZIF solids with different topologies and different linkers. The discrepancies obtained between the experimental data and simulation results by using our force field are still less important than those observed by using other force fields available in the literature.

Adsorption sites: To understand better the main adsorption sites observed for the different ZIF materials, we have calculated potential energy surfaces (PES) representing the different energy contributions (vdW and electrostatics) exerted by the different host frameworks on the adsorbed molecules.

The main adsorption sites, represented by the location of the center of mass of CH_4 (303 K, 5 bar) and CO_2 (303 K, 50 bar) on ZIF-8, are shown in Figure 7a and b, respectively. In ZIF-8 the most energetically favorable locations for adsorption are regions close to the imidazole rings. In fact, the Zn atoms are quite far from the accessible surface for guest molecules ($d_{m-s}=0.35$ nm; see Table 2). This is significantly different from the situation in common MOF structures, in which the most energetic adsorption sites are close to the oxygen atoms of bicarboxylic linkers around the metallic clusters. Our calculations agree with a recent experimental study in which the main adsorption sites for CH_4 in ZIF-8 were determined by neutron powder diffraction (NPD), difference Fourier, and Rietveld analysis.[32] We can superimpose the sites reported in Ref. [32] on the CH_4 adsorption sites in Figure 7a. In addition, we observe that the main adsorption sites perfectly match the regions where the vdW interactions are maximal, as revealed by the PES in Figure 7c. For instance, the preferential sites for vdW interactions are inside the sodalite cage, close to the methyl groups of the mIm linkers (site I), and on both sides of the center of the six-membered-ring windows (site II).

The preferential adsorption sites for electrostatic interactions are on both sides of six-membered-ring windows (similar to site II) and in the middle of the faces of the accessible surface area of ZIF-8 (site III), which is close to the aromatic rings of the mIm linker that is above the center of the four-membered ring (as shown by the arrows in Figure 7b and d). Sites III cannot be described by the vdW energy but correspond to the regions where the electrostatic interactions are maximal (Figure 7d). The last adsorption site reported in Ref. [32], placed in the middle of the ZIF-8 cavity, is also present in our simulations at high loading, particularly for the case of CO_2 (not shown). However, this site cannot be explained by host–guest interactions and is the result of a preferential arrangement between adsorbed guest molecules.

In Figure 8 we have extended this analysis to ZIF-69. The particular topology of the solid shows two different unconnected channels with pores that are accessible for both CH_4 and CO_2 molecules. The arrangement of organic linkers induces an important segregation of energy interactions of different kinds. For instance, the analysis of the vdW PES allows the identification of several regions with preferential interaction energies. The largest channels (formed mainly by cbIm linkers pointing to the center of the cavity) have important regions with strong vdW interactions (Figure 8a). The small channel (formed by nIm linkers with the NO_2 groups pointing toward the pores of the cavity) shows strong electrostatic interactions (Figure 8b). The combination of

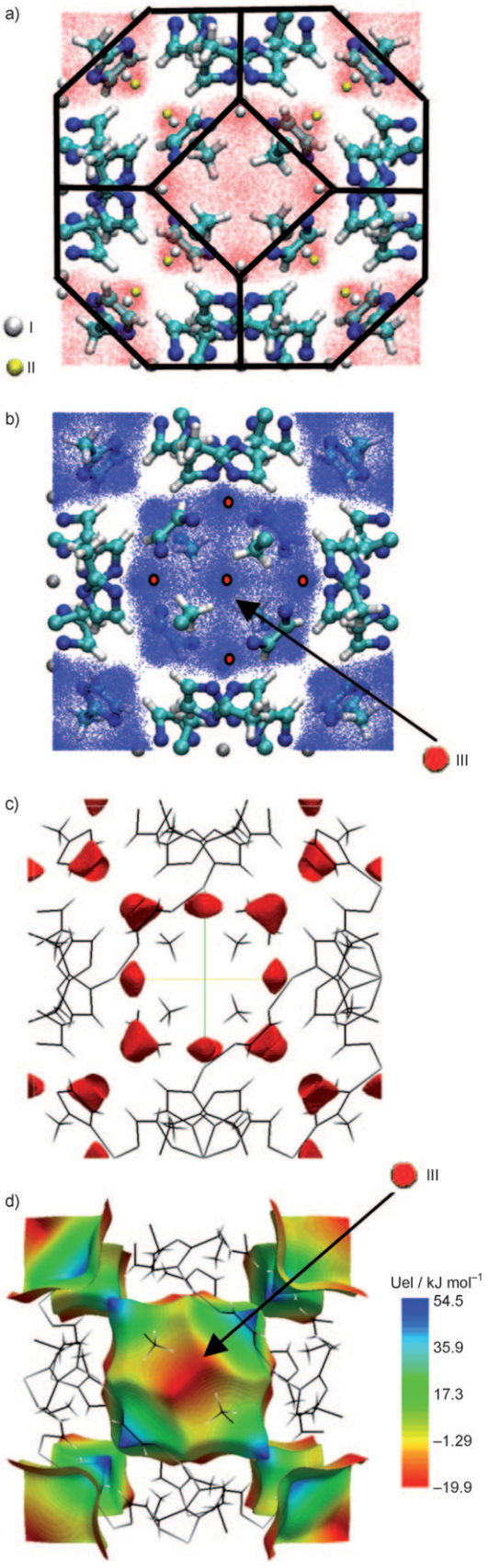

Figure 7. Representation of the center of mass of a) CH_4 and b) CO_2 molecules adsorbed on ZIF-8 at 303 K and 5 bar. c) Location of sites for maximum vdW interaction in ZIF-8. d) Projection of the electrostatic interactions of a positive charge (+1) over the accessible surface area. The lines in (a) represent the typical SOD topology. Atoms: Zn (gray), C (cyan), N (blue), and H (white).

Table 2. Comparison of Henry constants (H_E) at 303 K and isosteric heat of adsorption (q_{st}^0) at zero loading computed for CO_2, CH_4, and N_2 molecules adsorbed on the different ZIF materials.[a]

ZIF	U_{vdW}[b] [kJ mol^{-1}]	U_{el}[c] [kJ mol^{-1}]	d_{m-s}[d] [nm]	H_E [10^2 mol m^{-3} Pa^{-1}] $CO_2/CH_4/N_2$	q_{st}^0 [kJ mol^{-1}] $CO_2/CH_4/N_2$
ZIF-8	−15.2	+54/−20	0.35	0.51/0.28/0.10	(NA/12.0/NA)[e] 15.93/12.44/9.83
ZIF-69	−19.5	+171/−239	0.33	(2.64/0.59/0.15)[f] 1.53/0.40/0.13	(22.68/18.88/13.78)[f] 23.10(29.04)[g]/15.52/12.05
ZIF-76	−14.8	+325/−200	0.20	1.86/0.22/0.11	25.1/11.53/9.68

[a] Experimental values in parentheses. [b] Maximum value of vdW interaction energy on the preferential adsorption sites for CH_4 molecules. [c] Maximum values of the electrostatic energy of a positive charge (+1) interacting with the solid over the accessible surface area. [d] Minimal distance between the metal atoms and the accessible surface. [e] Experimental data from Ref. [7]. NA: experimental data not available. [f] Experimental data extracted from the gas isotherms at 298 K reported in Ref. [11]. [g] Simulation result from Ref. [30] computed at 273 K.

these two types of interactions makes it possible to identify five potential adsorption sites (Figure 8c). Sites I and II are placed on the central channel, close to the cbIm linkers. Sites III are placed on the windows connecting the pores of the small channels, whereas sites IV are placed on the small (and nonporous) windows connecting the two channels. Finally, sites V are placed in a trigonal symmetry close to the nIm linkers in the small channels.

The distribution of adsorbed CO_2 molecules at 303 K and 5 bar (Figure 8d) confirms the adsorption sites previously listed. The adsorption of CO_2 molecules in ZIF-69 is much more localized than in ZIF-8. The results reported in Ref. [30] for the center-of-mass probability distribution of CO_2 adsorbed on ZIF-69 are in agreement with our energy analysis.

Note that, at low pressure, CO_2 molecules are first adsorbed in the large channels and then secondly in the small channels. We notice that CO_2 molecules adsorbed in the small channels (connecting two pores) are forcibly aligned with the pore. The explanation for this behavior may come from an entropy loss in the system under these conditions, which is not compensated by the strong electrostatic energy observed inside these channels (see Figure 8b). Our results differ from the findings reported in Ref. [30], in which the authors observe that the small channels are the preferential adsorption sites for CO_2 at low pressures. For the adsorption of CH_4 at low pressures, we observed a non-negligible population of adsorbed molecules on these regions (see the Supporting Information). This difference occurs because CH_4 molecules fit the small channels better, without any preferential orientation. In general, as in the case of ZIF-8, the preferred adsorption sites are situated either close to the substituents of the imidazole linker or close to windows connecting two pores.

The analysis of preferential sites becomes more complex for ZIF-76. The PES for vdW interactions shows a complex topology (Figure 9a). In this case, regions with maximum energy interactions distributed in the material are not symmetric, owing to the irregular distribution of the cbIm linkers. Taking into account the vdW and electrostatic contributions shown in Figure 9a and b, we can identify three main regions of maximum interactions: 1) inside the double four-membered rings (D4R) connecting the sodalite cages, which are not accessible for adsorbed gases (I, see the Supporting Information); 2) inside the LTA supercage or main cavity facing the Im linker that connects the supercage with the double rings (II); 3) around the windows connecting two supercages and facing the aromatic rings of cbIm linkers (III, Figure 9b). In this case the electrostatic interactions are stronger than in the other two materials studied in this work.

Figure 9c, which illustrates the configurations of CH_4 molecules adsorbed at 303 K and 5 bar, shows that molecules are preferentially adsorbed in region II (inside the LTA supercage) and close to the windows connecting the supercage with the sodalite cages. Figure 9d shows CO_2 molecules adsorbed on ZIF-76 in similar thermodynamic conditions. In this case, molecules are strongly adsorbed at the windows connecting LTA supercages (region III). Adsorption is also important at the linkers connecting the sodalite cages and the LTA supercage. This fact is qualitatively similar to the distribution of adsorbed molecules in LTA zeolites.[33] Note that adsorption in region III is more important in ZIF-76 than in LTA zeolites.

The proposed methodology, employing potential-energy surfaces of the different host–guest contributions, appears to be a good approach to understanding the main adsorption sites of ZIF materials. We think that this approach can be extended to other types of MOFs and zeolites.

Role of metal sites and electrostatics: Recent studies have shown that CO_2 adsorption on standard MOFs is weakly influenced by the electrostatic interactions.[34] This situation changes when zeolite-like MOFs are considered. The influence of the electrostatic interactions over the CO_2 adsorption on ZIF-8, ZIF-69, and ZIF-76 can be observed in Figure 10a. At low loadings there are large relative deviations from the case in which full host–guest interactions were considered, in particular for ZIF-76 (approximately 78%) and ZIF-69 (approximately 65%), but at high pressures (or loading) the deviations decrease to 20%. ZIF-8 is less affected by the electrostatic contribution than the other two solids, as can be expected from the magnitude of the electrostatic PES (see Table 2). At high pressure, fluid–fluid interactions become important and the absence of electrostatic host–guest interactions is not as important as in the low-pressure regime, under which the energy of the system is practically dominated by the host–guest interactions.

One important question arises when analyzing the adsorption on ZIF materials: what role do metals play in adsorption? Considering the minimal distance observed between metals and the accessible surface area for the different ZIFs

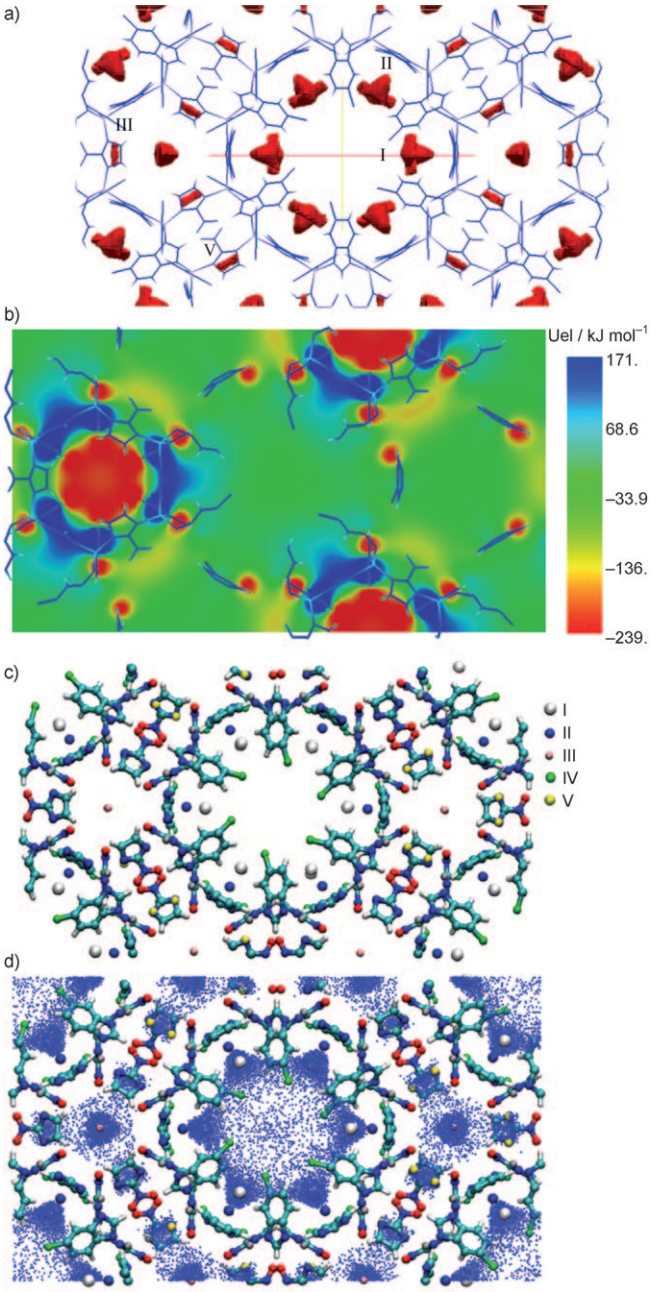

Figure 8. a) Location of the sites for maximum vdW interaction in ZIF-69. b) Projection of the electrostatic interactions of a positive charge (+1) over a plane intersecting the two types of pores of ZIF-69. c) Schematic representation of the main adsorption sites on ZIF-69. d) Representation of the center of mass of CO_2 molecules adsorbed on ZIF-69 at 303 K and 5 bar. Atoms: Zn (gray), C (cyan), N (blue), H (white), Cl (green), and O (red).

analyzed here (see Table 1), we can guess that adsorption should not be strongly affected by metals as far as vdW interactions are concerned. The influence of the vdW interactions of metal sites has been investigated by removing these energy contributions, as demonstrated in Figure 10b for different ZIFs. This figure reveals that for all the solids studied in this work, the deviations are less than 10% at different pressures. The contribution of the vdW interactions of

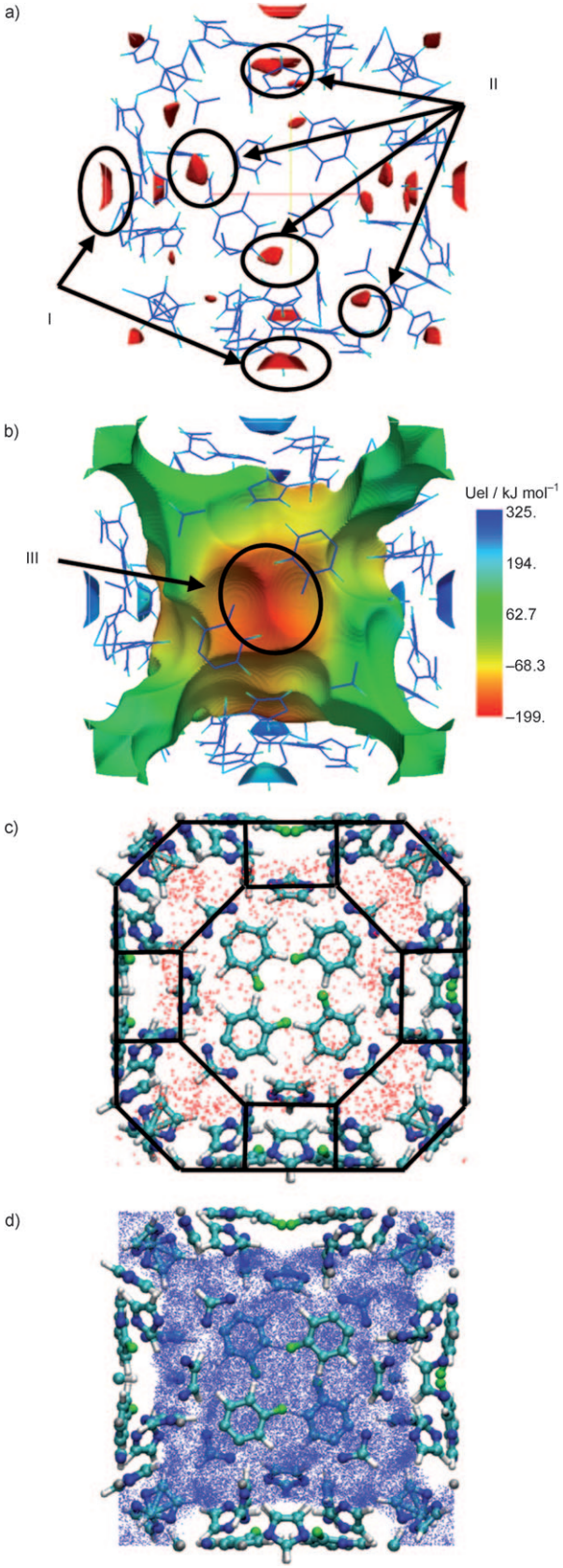

Figure 9. a) Location of the sites with maximum vdW interaction in ZIF-76. b) Projection of electrostatic interactions of a positive charge (+1) over the accessible surface area. Representation of the center of mass of molecules adsorbed on ZIF-76: c) CH_4 at 303 K and 5 bar and d) CO_2 at 303 K and 50 bar. The lines in (c) represent the typical LTA topology. Atoms: Zn (gray), C (cyan), N (blue), H (white), and Cl (green).

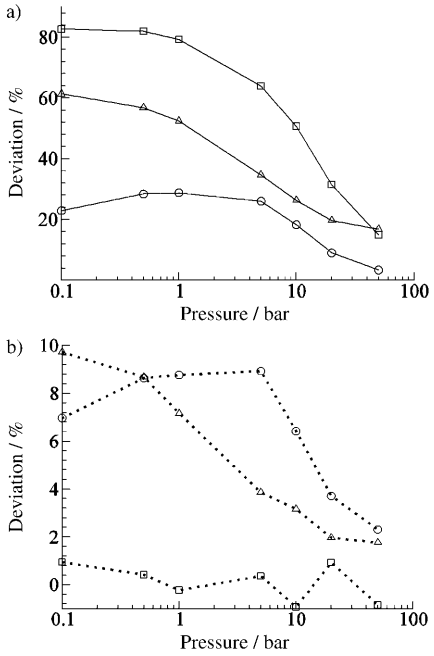

Figure 10. Deviation observed on absolute adsorption of CO_2 for ZIF-8 (○), ZIF-69 (△), and ZIF-76 (□) at 303 K when a) no electrostatic interactions are considered for host–guest interactions and b) no vdW interactions are considered for Zn metal. The results are expressed in relative deviation (%) from the number of molecules adsorbed in the case of full host–guest interactions.

metals becomes even less important at higher pressures, so the behavior of ZIFs is similar to that of normal zeolite structures, in which guest-Si–vdW and guest-Al–vdW contributions are commonly ignored in adsorption modeling by molecular simulations.

Adsorption thermodynamics: The last part of our analysis was devoted to the thermodynamic behavior of adsorbed molecules on ZIF materials. Simulation results for Henry constants (H_E) and isosteric heats of adsorption (q_{st}^0) at zero coverage computed for CO_2, CH_4, and N_2 molecules adsorbed on the different solids are compiled in Table 2. The calculated Henry constants and heats of adsorption are in agreement with the experimental data for ZIF-8 ($q_{st}^0(CH_4) = 12.0\ kJ\,mol^{-1}$)[7] and ZIF-69 ($q_{st}^0(CO_2) = 22.7\ kJ\,mol^{-1}$; $q_{st}^0(CH_4) = 18.9\ kJ\,mol^{-1}$; $q_{st}^0(N_2) = 13.8\ kJ\,mol^{-1}$).[11] Our results were also coherent with other simulation results for the case of CO_2 adsorption on IRMOF and COF materials.[35] Henry constants and heats of adsorption of CH_4 and N_2 follow the order ZIF-76 ≈ ZIF-8 < ZIF-69. Surprisingly, the cbIm linkers in ZIF-76 do not significantly contribute to increasing the Henry constant compared with ZIF-8. This may be because we probably underestimate the vdW interactions of the cbIm linkers, as previously mentioned in our comparative analysis of the adsorption behavior.

The highest Henry constants and heats of adsorption are observed for ZIF-69. As discussed above, the smaller pore size of this solid increases the confinement and, therefore, leads to a stronger vdW interaction. This confinement effect can be quantified by looking at the minima of the vdW PES of the three solids (Table 2). The deepest vdW potential-energy well in ZIF-69 is $-19.5\ kJ\,mol^{-1}$, whereas the strongest vdW interaction of ZIF-76 and ZIF-8 is only about $-15\ kJ\,mol^{-1}$. These minima of the vdW PES perfectly correlate with the heats of adsorption of CH_4 and N_2, which confirms that vdW interactions govern the adsorption behavior of the two molecules (see the Supporting Information).

In the case of CO_2, not only vdW but also electrostatic interactions have to be taken into account. The orders of the Henry constants and of the heats of adsorption, therefore, deviate from those of CH_4 and N_2: ZIF-76 has the strongest interaction with CO_2 at low pressure, followed by ZIF-69 and ZIF-8. This can again be explained by examining the electrostatic potential-energy surface. ZIF-76 has the strongest electrostatic field of the three samples, which strongly increases its interaction with CO_2, especially when compared with ZIF-8. The simulated adsorption isotherms of CH_4 on ZIF-76 and ZIF-8 are quite similar, whereas the adsorption of CO_2 on ZIF-76 is much stronger. The peculiar behavior observed for ZIF-76 can also be explained by the fact that Zn atoms are much more exposed to the accessible surface area than the other two ZIFs analyzed (see Table 2). This may explain the strongest electrostatic interactions on the PES observed in Figure 9b.

The orders of magnitude obtained for q_{st}^0 for CO_2, CH_4, and N_2 on ZIFs are comparable to the values obtained on silicalite[36] and MOF materials,[35] and are considerably lower than those obtained for ion-exchanged zeolites.[37]

Conclusion

We have investigated both experimentally and by molecular simulation the adsorption behavior of N_2, CH_4, and CO_2 on two different zeolitic imidazolate frameworks, ZIF-8 and ZIF-76. Our simulation results reveal the lack of accuracy when standard force fields are used to reproduce our experimental data as well as other data available in the literature. A new force field, based on a modified version of the UFF, describing the host–guest framework interactions of CH_4 adsorbed on ZIF-8 has been proposed. The transferability of the proposed force field was confirmed by comparing simulation results with the available experimental data for different gases (CO, CO_2, CH_4, and N_2) and solids (ZIF-69 and ZIF-76). The approach used to derive the intermolecular potential model (based on the UFF) preserves the general use of our force field to screen the behavior of gas adsorption on different MOF materials with imidazolate linkers.

The new force field has been used to analyze the preferential adsorption sites for the different solids and gases by means of host–guest potential-energy surfaces. Our results confirm the main adsorption sites for CH_4 on ZIF-8 that were recently reported and were obtained by neutron powder diffraction (NPD), difference Fourier analysis, and

Rietveld analysis:[32] in general, preferential adsorption sites are located in specific regions close to the organic imidazolate linker, and not on the metal atoms. This contrasts with the behavior of several MOFs in which the preferential adsorption site is not on the organic linker, but on the metal center.[38]

Suppression of the vdW interactions of metal atoms upon gas adsorption shows that they contribute less than 10% to the total amount adsorbed. Our results confirmed that metals play a similar role on ZIFs to that of Si and Al atoms on normal zeolites, mainly contributing by their electrostatic interactions. The electrostatic interactions on ZIFs are crucial to reproduce the behavior observed on experimental CO_2 adsorption isotherms. This fact makes ZIFs substantially different from other MOF structures as far as CO_2 adsorption is concerned, in which case this interaction could be neglected.

Henry constants and isosteric heats of adsorption have been computed for CO_2, CH_4, and N_2 on ZIF-8, ZIF-69, and ZIF-76. The values obtained are considerably lower than those observed for normal zeolites, with the exception of silicalite. In general, the orders of magnitude obtained for these two properties are similar to those reported for MOFs based on dicarboxylic acids. The variations of the Henry constants and the isosteric heat of adsorption for CO_2, CH_4, and N_2 on different solids have been successfully correlated with the differences in host–guest energy interactions as revealed by the PES analysis. As expected, the adsorption of CH_4 and N_2 is totally controlled by the vdW interactions, whereas for CO_2 both vdW and electrostatic interactions play a role, the latter being dominant.

Experimental Section

Synthesis of ZIF-8: ZIF-8 was synthesized by the procedure reported by Huang et al.[2] with slight modifications to address the question of larger-scale production of this material. 2-Methylimidazole (32.21 g, Sigma–Aldrich, 99%) was dissolved in methanol (500 mL, SDS, HPLC grade 99.8%). This solution was added to the synthesis reactor containing a solution of $Zn(OH)_2$ (19.52 g, International Laboratory, 95%) in aqueous ammonia (2.5 L, Carlo–Erba, 25%) through a peristaltic pump (Masterfex, flow rate 6 mL min^{-1}). Synthesis was performed at ambient temperature, with gentle stirring (150 rpm) in a reactor (3 L) equipped with baffles. A white solid was collected, washed three times with methanol/water (1:1 v/v, 3×500 mL), dried in air, and characterized by XRD and N_2 adsorption isotherms.

Synthesis of ZIF-76: ZIF-76 synthesis was on a smaller scale. In a vial (20 mL), imidazole (1.52 mmol) and 5-chlorobenzimidazole (0.76 mmol) were dissolved in a solution of DMF/diethylformamide (50:50 v/v, 10 mL). $Zn(NO_3)_2{\cdot}6H_2O$ (0.79 mmol) was added to the mixture and the solution was stirred for 10 min. NaOH (2.5 mol L^{-1}, 1.14 mmol) was added and the vial was heated to 363 K for five days, to give white crystals (yield = 76% based on zinc). The product was isolated by filtration, washed with DMF, and dried at 343 K for 1 h. Its purity was verified by powder XRD and N_2 adsorption isotherms. Comparison of the experimental and the simulated XRD patterns, by using the reported crystal structures of ZIF-8 and ZIF-76, is provided in the Supporting Information.

Adsorption measurements: The high-pressure adsorption isotherms of CH_4, CO_2, and N_2 were measured by using a Rubotherm magnetic suspension balance. ZIF materials (0.2–1.4 g) were first activated under vacuum at 473 K for 4–8 h. The volume, and hence the skeleton density, of the samples were then determined by measuring the apparent mass of the sample as a function of pressure in a He atmosphere at 303 K. Then, the adsorption and desorption isotherms of CH_4, CO_2, and N_2 were recorded in the range 0.2–40 bar at 303 K. After each isotherm determination the sample was regenerated by treatment at 473 K under vacuum. The measured apparent mass of the sample was corrected for the buoyancy of the sample (known from the skeleton density) and the sample holder, that is, $\rho_{gas}(V_{sample}+V_{sample\ holder})$. Although the density of the gas could be measured in situ, the precision of the measured values was not always satisfactory. We, therefore, preferred to deduce ρ_{gas} from the Peng–Robinson equation of state. The adsorbed amounts after buoyancy correction represent excess adsorbed amounts.

Computational methods

Model parameterization: Many theoretical studies focus on simulation of the adsorption phenomena of different gases on MOF materials. In particular, the CVFF with Dreiding refitted parameters has been used to reproduce structural properties correctly such as the peculiar negative thermal expansion or CO_2 sorption isotherms on IRMOF-1.[23] Other rigid force fields have been used to reproduce adsorption isotherms. For instance, Yang and Zhong[21] reproduced the adsorption of CO_2 and CH_4 on IRMOF-1 by using different parameter sets depending on the adsorbate molecule. This approach unfortunately lacks transferability. The UFF-based parameters used by Babarao et al.[17] overcome this problem by reproducing the isotherms of both CO_2 and CH_4 with a unique set of parameters. Previous calculations[31] revealed that the standard force fields (CVFF, UFF, Dreiding) were unable to reproduce the form of the CH_4 isotherm on ZIF-8 when compared with the available experimental data[7] as well as with our own experiments. We, therefore, decided to adjust the force-field parameters of the methyl imidazolate linkers in ZIF-8 to obtain a better match between simulation and experimental data.

Several specific force fields in the literature provide parameters to reproduce the intermolecular interactions of the imidazolate rings.[39,40] However, these force fields were optimized to consider phase equilibrium and they are not well adapted to reproduce the adsorption phenomena on 3D structures. We used the Lennard-Jones (LJ) parameters of the UFF force field as the starting point of our optimization procedure. The LJ parameters based on this force field were readapted by scaling cohesive energy on the dispersion–repulsion interactions as in [Eq. (2)], in which σ_{ij} and ε_{ij} are the crossed LJ parameters obtained between the solid parameters and the methane model of Moller et al.[41]

$$(\varepsilon_{ij}\sigma_{ij}^6)_{New} = \zeta(\varepsilon_{ij}\sigma_{ij}^6)_{UFF} \quad (2)$$

Crossed LJ interactions were calculated by applying standard Lorentz–Berthelot combining rules. The parameter ξ was then determined by an iterative procedure to fit the experimental CH_4 isotherm of ZIF-8 at 303 K. Methane was chosen because electrostatic interactions can be safely neglected. In particular, special attention was paid to reproduction of the low-pressure limit of the isotherm in which host–guest interactions are dominant.

Potential-energy surfaces: The potential-energy surfaces for vdW and electrostatic interactions have been computed by numerical evaluation of the energy grids that were used for adsorption calculations. In the first case (vdW), the PES was obtained from the interaction of a ghost methane particle with the solid structure by using the optimized parameters of our force field (alternatively, a He atom can be used). The isosurface of the accessible area, which according to Düren et al.[12] is slightly different from the Connolly surface, can be computed by rolling a methane sphere over the vdW grid. We have proceeded in a different manner because the location of the accessible isosurfaces have been determined by 3D map-

ping through the Paraview version 3.4 package,[42] finding the ensemble of points Γ where the vdW interaction energy becomes just repulsive ($U_{vdW}(\Gamma)=0$). For the electrostatic surfaces we have also used the electrostatic grid computed for the adsorption process and have evaluated with a hypothetical methane particle with a positive charge of +1. This evaluation does not preserve the electroneutrality of the system, but the objective of this plot is not to perform simulations of molecular adsorption (as it should be for the isotherm calculations) but only to qualitatively reveal the surfaces of the solid which are most strongly charged. The accessible surface area projected with the electrostatic interactions was calculated by using the Paraview software. This kind of plot can help in the recognition of the regions over the surface of the solid where polar molecules could be preferentially adsorbed.

Simulation methods: Grand Canonical Monte Carlo (GCMC) simulations combined with a bias scheme[43] for the insertion of the center of mass of the guest molecules were performed to calculate the adsorption isotherms with the Gibbs code v.8.3.[44] A bias scheme was used for enhancing the acceptance rate of the insertions. The selected probabilities for the different moves were generally set to 0.35 for rigid-body translations, 0.10 for rigid-body rotations (only in the case of CO_2, N_2, and CO), and 0.55 for insertions or deletions. Systems were allowed to equilibrate for at least 10^6 MC steps, which were followed by production runs of at least 10^7 MC steps. The atomic positions of the solid were frozen during the simulations. This allowed construction of a host–guest interaction-energy grid before the MC simulations. All simulations were performed in a simulation box incorporating $2\times2\times2$ unit cells for ZIF-8 and ZIF-76, and $1\times2\times2$ unit cells for ZIF-69. The absence of size effects was verified by considering larger simulation boxes ($3\times3\times3$), but no significant differences in adsorption were observed. LJ interactions and real-space electrostatic contributions were calculated by using a cut off radius of ~17 Å. No LJ tail corrections were considered,[45] but standard long-range electrostatic interactions were calculated by using the Ewald methodology with ten vectors on the reciprocal space and a screening factor $n\alpha$ of 2.5. Crystallographic positions of the different atoms for all the ZIF materials were taken from the data available in the Cambridge Structural Database.[46] In the case of ZIF-76, the imidazolate linkers are partially occupied by cbIm. The partial occupation was dealt with by deleting part of the chlorobenzene ring manually so as to respect the ratio of cbIm/Im = 1:3 per Zn atom. The structure was then relaxed to avoid close contacts between two neighboring chlorobenzene rings. Three different structures were generated by exploring different positions and orientations of the organic linkers. Comparison of the experimental results of CH_4 at 303 K and simulation data obtained by using these different structures revealed that structural changes have a negligible impact on the final simulation results (see the Supporting Information for additional details). In our analysis we used the solid presenting the most favorable structural energy. The pores in ZIF-8 and ZIF-69 are fully accessible to methane molecules (and the other gases that were adsorbed in the course of this work). In the case of the D4R cages of ZIF-76, the adsorbed gases cannot access the pores. Consequently they were blocked by using dummy molecules, following a procedure used in the simulation of zeolites.[47,48] A comparison of methane isotherms in ZIF-76 with and without the blocking of the D4R cages is available in the Supporting Information.

The accessible volume of each solid was evaluated by means of the volume integral[17] in [Eq. (3)], in which U_{ads}^{He} is the LJ interaction between a single helium atom and the complete structure of the adsorbent (σ He = 2.58 Å, ε He = 10.22 K).

$$V_{free} = \int_V \exp\left(-U_{ads}^{He}(r)/k_B T\right) dr \quad (3)$$

In all our calculations the diameters of the framework atoms were taken from the optimized force field. The porosity ϕ is simply the ratio of the free volume V_{free} to the total volume of the unit cell V_{UC} as shown in [Eq. (4)].

$$\phi = \frac{V_{free}}{V_{UC}} \quad (4)$$

To determine the fugacities corresponding to the different pressure conditions, simulations in the isobaric–isothermal (NPT) ensemble combined with the particle-insertion method were performed.[49] In this case the selected probabilities for MC moves were set to 0.63 for rigid-body translations, 0.35 for rigid-body rotations (only in the case of CO_2, N_2, and CO), and 0.02 for volume changes. Bulk densities that were used to transform the absolute number of molecules adsorbed in the solid into excess quantities were also obtained from the NPT MC simulations. This transformation was done according to [Eq. (5)], in which N_{ex} and N_{abs} are the excess and absolute numbers of adsorbed particles, respectively, ρ_{bulk} is the density of the bulk gas calculated from the NPT simulations, and V_{free} is the free volume calculated from the interaction of a helium particle with the solid.[17] Details of the calculations of the free volume and surface area are given in the Supporting Information.

$$N_{ex} = N_{abs} - \rho_{bulk} V_{free} \quad (5)$$

Isosteric heats of adsorption q_{st} were calculated from [Eq. (6)],[50] in which H_b is the enthalpy of the bulk phase and U_a is the energy of the adsorbed phase.

$$q_{st} = H_b - \left[\frac{\delta U_a}{\delta N}\right]_{T,V} \quad (6)$$

By using a fluctuations method with ideal gas assumptions under Henry's regime, the isosteric heats can be readily calculated from GCMC simulation according to [Eq. (7)], in which U_{ext}^s is the intermolecular energy of the adsorbed phase and N is the number of adsorbed molecules. The angle brackets denote averages in the grand canonical ensemble.

$$q_{st} = RT - \frac{\langle U_{ext}^s N\rangle - \langle U_{ext}^s\rangle\langle N\rangle}{\langle N^2\rangle - \langle N\rangle^2} \quad (7)$$

To consider electrostatic interactions between the solid framework and guest molecules, we have determined the electrostatic potential interaction of the different ZIF materials. Partial atomic charges were computed from first-principle calculations at the level of the DFT[51] over cluster structures. In this work, the ESP[52,53] fitting methodology has been used. In this case the electrostatic potential was computed on a grid formed by merging sets of spherical shells, the grid points of which were centered on each atomic nucleus. The B3LYP functional was used in combination with the pseudopotential LanL2DZ[54] for the transition metal and the double-ζ basis set 6.31G** for the rest of the atoms.[55] All calculations were performed with the Jaguar package.[56] Additional details of the different force fields that were used to describe the adsorbed molecules and of the DFT calculations can be found in the Supporting Information.

Acknowledgements

The authors would like to acknowledge Sandrine Carl and Jean-Pierre Courcy for their assistance in the synthesis of ZIF-8 and the adsorption measurements on the ZIF samples.

[1] M. Eddaoudi, J. Kim, N. Rosi, D. Vodak, J. Wachter, M. O'Keeffe, M. Yaghi, *Science* **2002**, *295*, 469–472.
[2] X. C. Huang, Y. Y. Lin, J. P. Zhang, X. M. Chen, *Angew. Chem.* **2006**, *118*, 1587–1589; *Angew. Chem. Int. Ed.* **2006**, *45*, 1557–1559.
[3] Y. Liu, V. C. Kravtsov, R. Larsen, M. Eddaoudi, *Chem. Commun.* **2006**, *14*, 1488–1490.
[4] Y. Q. Tian, Y. M. Zhao, Z. X. Chen, N. G. Zhang, L. H. Weng, D. Y. Zhao, *Chem. Eur. J.* **2007**, *13*, 4146–4154.
[5] T. Wu, X. Bu, R. Liu, Z. Lin, J. Zhang, P. Feng, *Chem. Eur. J.* **2008**, *14*, 7771–7773.
[6] K. S. Park, Z. Ni, A. P. Côté, J. Y. Choi, R. Huang, F. J. Uribe-Romo, H. K. Chae, M. O'Keeffe, O. M. Yaghi, *Proc. Natl. Acad. Sci. USA* **2006**, *103*, 10186–10191.

[7] W. Zhou, H. Wu, M. R. Hartman, T. Yildirim, *J. Phys. Chem. C* **2007**, *111*, 16131–16137.
[8] H. Hayashi, P. A. Côté, H. Furukawa, M. O'Keeffe, O. M. Yaghi, *Nat. Mater.* **2007**, *6*, 501–506.
[9] H. Hayashi, P. A. Côté, H. Furukawa, M. O'Keeffe, O. M. Yaghi, *Nature* **2008**, *453*, 207–212.
[10] R. Banerjee, A. Phan, B. Wang, C. Knobler, H. Furukawa, M. O'Keeffe, O. M. Yaghi, *Science* **2008**, *319*, 939–943.
[11] R. Banerjee, H. Furukawa, D. Britt, C. Knobler, M. O'Keeffe, O. M. Yaghi, *J. Am. Chem. Soc.* **2009**, *131*, 3875–3877.
[12] T. Düren, R. Q. Snurr, *J. Phys. Chem. B* **2004**, *108*, 15703–15708.
[13] L. Sarkisov, T. Düren, R. Q. Snurr, *Mol. Phys.* **2004**, *102*, 211–221.
[14] T. Düren, L. Sarkisov, O. M. Yaghi, R. Q. Snurr, *Langmuir* **2004**, *20*, 2683–2689.
[15] J. Jiang, S. Sandler, *Langmuir* **2006**, *22*, 5702–5707.
[16] S. Wang, *Energy Fuels* **2007**, *21*, 953–956.
[17] R. Babarao, Z. Hu, J. Jiang, *Langmuir* **2007**, *23*, 659–666.
[18] N. A. Ramsahye, G. Maurin, S. Bourrelly, P. L. Llewellyn, T. Loiseau, G. Férey, *Phys. Chem. Chem. Phys.* **2007**, *9*, 1059–1063.
[19] N. A. Ramsahye, G. Maurin, S. Bourrelly, P. L. Llewellyn, T. Loiseau, C. Serre, G. Férey, *Chem. Commun.* **2007**, *31*, 3261–3263.
[20] F. Salles, A. Ghoufi, G. Maurin, R. G. Bell, C. Mellot-Draznieks, G. Férey, *Angew. Chem.* **2008**, *120*, 8615–8619; *Angew. Chem. Int. Ed.* **2008**, *47*, 8487–8491.
[21] Q. Yang, C. Zhong, *J. Phys. Chem. B* **2006**, *110*, 17776–17783.
[22] Q. Yang, C. Zhong, *ChemPhysChem* **2006**, *7*, 1417–1421.
[23] D. Dubbeldam, K. S. Walton, D. E. Ellis, R. Q. Snurr, *Angew. Chem.* **2007**, *119*, 4580–4583; *Angew. Chem. Int. Ed.* **2007**, *46*, 4496–4499.
[24] S. L. Mayo, B. D. Olafson, W. A. Goddard, *J. Phys. Chem.* **1990**, *94*, 8897–8909.
[25] A. K. Rappe, C. J. Casewit, K. S. Colwell, W. A. Goddard, W. M. Skiff, *J. Am. Chem. Soc.* **1992**, *114*, 10024–10035.
[26] P. Dauber-Osguthorpe, V. A. Roberts, D. J. Osguthorpe, J. Wolff, M. Genest, A. T. Hagler, *Proteins Struct. Funct. Genet.* **1988**, *4*, 31–47.
[27] D. S. Coombes, F. Cora, C. Mellot-Draznieck, R. G. Bell, *J. Phys. Chem. C* **2009**, *113*, 544–552.
[28] M. Tafipolsky, R. Schmid, *J. Phys. chem. B* **2009**, *113*, 1341–1353.
[29] Q. Yang, C. Zhong, J. F. Chen, *J. Phys. Chem. C* **2008**, *112*, 1562–1569.
[30] D. Liu, C. Zheng, Q. Yang, C. Zhong, *J. Phys. Chem. A* **2009**, *113*, 5004–5009.
[31] D. Fairen-Jimenez, P. Lozano-Casal, T. Düren in *Characterisation of Porous Solids VIII. Proceedings of the 8th International Symposium on the Characterisation of Porous Solids*, RSC, Cambridge, **2008**, pp. 80–87.
[32] H. Wu, W. Zhou, T. Yildirim, *J. Phys. Chem. C* **2009**, *113*, 3029–3035.
[33] R. Krishna, J. M. van Baten, *Sep. Purif. Technol.* **2008**, *61*, 414–423.
[34] K. S. Walton, A. R. Millward, D. Dubbeldam, H. Frost, J. J. Low, O. M. Yaghi, R. Q. Snurr, *J. Am. Chem. Soc.* **2008**, *130*, 406–407.
[35] R. Babarao, J. Jiang, *Langmuir* **2008**, *24*, 6270–6278.
[36] J. A. Dunne, R. Mariwala, M. Rao, S. Sircar, R. J. Gorte, A. L. Myers, *Langmuir* **1996**, *12*, 5888–5895.
[37] J. Zhang, R. Singh, P. A. Webley, *Microporous Mesoporous Mater.* **2008**, *111*, 478–487.
[38] H. Wu, W. Zhou, T. Yildirim, *J. Am. Chem. Soc.* **2009**, *131*, 4995–5000.
[39] N. Rai, I. J. Siepmann, *J. Phys. Chem. B* **2007**, *111*, 10790–10799.
[40] N. A. McDonald, W. L. Jorgensen, *J. Phys. Chem. B* **1998**, *102*, 8049–8059.
[41] D. Moller, J. Oprzynski, A. Muller, J. Fischer, *Mol. Phys.* **1992**, *75*, 363–378.
[42] Paraview version 3.4, http://www.paraview.org.
[43] A. D. Mackie, B. Tavitian, A. Boutin et A. H. Fuchs, *Mol. Simul.* **1997**, *19*, 1–15.
[44] P. Ungerer, C. Nieto-Draghi, V. Lachet, A. Wender, A. di Lella, A. Boutin, B. Rousseau, A. Fuchs, *Mol. Simul.* **2007**, *33*, 287–304.
[45] M. P. Allen, D. J. Tildesley in *Computer Simulation of Liquids*, Oxford University Press, New York, **1989**.
[46] The Cambridge Crystallographic Data Centre www.ccdc.cam.ac.uk/data_request/cif.
[47] G. Maurin, P. Lewellyn, T. Poyet, B. Kuchta, *J. Phys. Chem. B* **2005**, *109*, 125–129.
[48] E. Jaramillo, M. Chandross, *J. Phys. Chem. B* **2004**, *108*, 20155–20159.
[49] D. Frenkel, B. Smit in *Understanding Molecular Simulation: From Algorithms to Applications*, Academic Press, San Francisco, **2001**.
[50] T. Vuong, P. A. Monson, *Langmuir* **1996**, *12* , 5425–5432.
[51] P. Hohenberg, W. Kohn, *Phys. Rev.* **1964**, *136*, B864–B871.
[52] L. E. Chirlian, M. M. Francl, *J. Comput. Chem.* **1987**, *8*, 894–905.
[53] R. J. Woods, M. Khalil, W. Pell, S. H. Moffat, V. H. Smith, *J. Comput. Chem.* **1990**, *11*, 297–310.
[54] P. J. Hay, W. R. Wadt, *J. Chem. Phys.* **1985**, *82*, 299–310.
[55] R. Ditchfield, W. J. Hehre, J. A. Pople, *J. Chem. Phys.* **1971**, *54*, 724–728.
[56] Jaguar version 7.0, Schrödinger, LLC, New York, **2007**.

Received: August 1, 2009
Published online: December 8, 2009

